Crimson Publishers
Wings to the Research

Review Article

Analysis and Study of the Dynamics and Aerodynamic Characteristics of Catapulted Small Guided Vehicles

Chengge Liu*

College of Mechanical Engineering, Zhejiang University, China

ISSN: 2640-9690

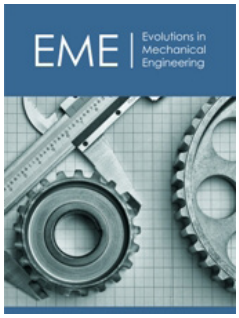

Abstract

The small vehicle is ejected from the launcher using a catapult and strikes the target bull's-eye following a parabolic flight. Modal analysis of the vehicle is conducted to avoid resonance before launch, which could affect the flight trajectory. In-flight flow field analysis is performed to study the vehicle's flight attitude. Upon hitting the target, a strong impact is expected and landing will result in a significant collision. When the vehicle falls to the ground, it may be crushed by a wheeled robot. Finite element analysis is used to study the stress on the parts most likely to fracture, so they can be reinforced accordingly.

Keywords: ANSYS; Modal analysis; Flow field analysis; Collision analysis; Stress analysis

***Corresponding author:** Chengge Liu, College of Mechanical Engineering, Zhejiang University, Hangzhou, China

Submission: January 06, 2025
Published: February 11, 2025

Volume 5 - Issue 5

How to cite this article: Chengge Liu*. Analysis and Study of the Dynamics and Aerodynamic Characteristics of Catapulted Small Guided Vehicles. Evolutions Mech Eng. 5(5). EME.000624. 2025.
DOI: 10.31031/EME.2025.05.000624

Introduction

Small guided vehicles have shown great potential for applications in many missions, such as reconnaissance, communications relay, precision strike, battlefield damage assessment and electronic jamming, duo to their advantages of rapid response, diversified launching tools, flexible launching locations and low cost. With the increasing demand for integrated reconnaissance, strike and damage assessment functions for precision-guided weapons, small vehicle technology is rapidly becoming a research focus [1]. Dynamic analysis and aerodynamic characterization are key foundations for the design and optimization of small aircraft. In the international research field, advances in low Reynolds number aerodynamics have provided a new theoretical basis and technical support for the design of micro air vehicles. The study by Danupol S [2] explored the aerodynamic characteristics of a small UAV with a box-wing configuration through CFD simulations, demonstrating its advantages under low Reynolds number conditions. Aditya & Srinivas [3] summarised the recent research advances in low Reynolds number flyers, highlighting the importance of the study of low Reynolds number aerodynamics for improving the efficiency and performance of man-made vehicles. Furthermore, Ronan Serré & Nicolas Gourdain [4] developed a low-cost numerical method to achieve noise reduction by optimizing the geometry of the rotor blades of a microlight vehicle, and the experimental results showed a noise reduction of 8 dB(A) [4].

Domestic research has also made remarkable progress. Ang Haisong [5] analysed the effects of low Reynolds number and non-constant aerodynamic characteristics on MAVs and introduced the corresponding aerodynamic calculation methods and non-constant aerodynamic design software, emphasizing the key role of AI methods in enhancing the autonomy of MAVs. The experimental study by Zhang Fuxing [6] has thoroughly explored the aerodynamic characteristics of flexible-wing micro-vehicles under low Reynolds number conditions, which provides an important scientific foundation and technical support for the design of micro-vehicles. In addition, Wenqing Yang [7,8] presented new perspectives and solutions aimed at optimizing the aerodynamic performance and flight efficiency of the vehicle in their analysis of the research progress and challenges in the field of bionic

micro-flapping wing vehicles. This research provides a basis for the improvement of iterative guidance methods and derives a series of nonlinear guidance methods based on optimal control theory [9-15]. Literature [16] studied the launch vehicle guidance method based on the measurement of wind information, and literature [17] provided a unified comparison of the guidance methods in the ascent section. Through simulation calculations, the closed-loop guidance method based on the optimal control does not have outstanding advantages in improving the accuracy, and its advantages are more reflected in the ability to adapt to the constraints and further reflected in the improvement of reliability.

Subsequent research on guidance methods for the ascent segment of the launch vehicle has evolved towards the study of composite methods [18-20] and the improvement of the adaptability to constraints [21,22]. Research on the ascending segment of the Space Shuttle has also begun to focus on the ability to return to the launch site from a reliability standpoint [23,24] and a great deal of research has been carried out on fault-adaptive guidance methods [25-30]. Through the above research, it was found that although existing studies provide an important theoretical and practical basis, they still have limitations in dealing with vehicle launch and flight performance under specific conditions. In particular, the problem of uncertainty and conceptual confusion in conventional techniques limits the depth and breadth of research into accurately modelling the dynamic response and aerodynamic characteristics of aircraft in complex environments. Therefore, this study adopts the finite element method to comprehensively analyse the dynamics and aerodynamic characteristics of a catapulted small guided vehicle, aiming to solve the limitations of the traditional research methods and to improve the design efficiency and flight performance of small guided vehicles. This not only further deepens the understanding of the dynamics and aerodynamic characteristics during the launching process of small vehicles, but also provides a new theoretical basis and technical path for the design optimization of future vehicles.

Structural and Mechanical Analysis of Small Vehicles

Structural design

The object of the study is a catapult-type vehicle, and its application background is the Robo Master National University Robotics Competition. The vehicle is launched from a launcher at a designated location, and after gliding, it needs to hit the target with the head of the vehicle to be considered successful. As shown in Figure 1. The overall layout of the vehicle is similar to that of a fixed-wing UAV, with two controllable rudder wings on the main wing and one on the tail's drogue and one on the flat tail. The wing material is 1mm carbon fibre plate; The rudder wing material is resin, which is 3D printed; The aircraft fuselage material is fibre-added nylon, which is 3D printed in one piece. The 4 rudder wings are individually pulled by 4 rudder pull rods and the front of the craft is equipped with an OV7740 wide-angle 120-degree lens camera module. The entire small craft weighs in at 196g. Figure 2 shows the internal structure of a small guided vehicle and its main components:

Figure 1: Schematic illustration of the effective hit on the centre of gravity of a flight vehicle.

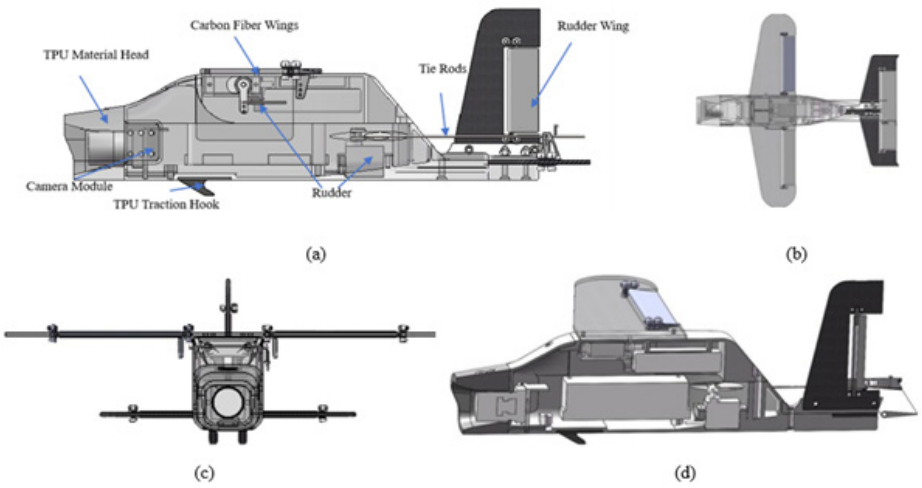

Figure 2: Small guided vehicle: (a) small guided vehicle left view; (b) small guided vehicle top view; (c) small guided vehicle main view; (d) small guided vehicle cutaway view.

a. Head made of TPU: the front part of the vehicle, which is made of thermoplastic polyurethane (TPU) material with good elasticity and impact resistance to mitigate the impact when the front part of the vehicle lands.

b. Camera module: A camera module located at the front of the vehicle for target identification and navigation. It may include a wide-angle lens to cover a larger field of view.

c. TPU towing hooks: Used to connect and fix the parts of the vehicle on the launcher to ensure the stability of the vehicle during launch.

d. Rudder: A device that controls the direction and attitude of the vehicle and achieves precision guidance by adjusting the angle of the rudder wing.

e. Carbon Fiber Wings: The main lift and control surfaces, made of lightweight and strong carbon fibre material, provide the necessary rigidity and durability.

f. Tie rods: The parts connecting the rudder and rudder wing are used to transmit the control instructions from the rudder so that the rudder wing can be adjusted accordingly.

g. Rudder wing: the control surface of the vehicle, which changes the flight trajectory of the vehicle by adjusting the angle to ensure precise guidance.

The design of the small guided vehicle combines a variety of advanced materials and technologies to achieve light weight, high strength and precise control. These characteristics enable the vehicle to perform reconnaissance, strike and other tasks in complex environments and have high practical value.

Hardware design for small craft

For the visual recognition solution, the OPENMV platform was chosen, using the low-cost STM32H750 as the vision processor and the OV7740 wide-angle 120-degree lens camera module as the recognition camera, which can achieve a recognition frame rate of 60FPS in practical use. The attitude control system and the visual recognition system communicate through a serial port to achieve end-to-end guidance. In the design of the control board of the vehicle, for the flight speed of the small vehicle, we carry a differential pressure sensor on the control board and also provide a macro-USB interface for debugging the microcontroller, as shown in Figure 3.

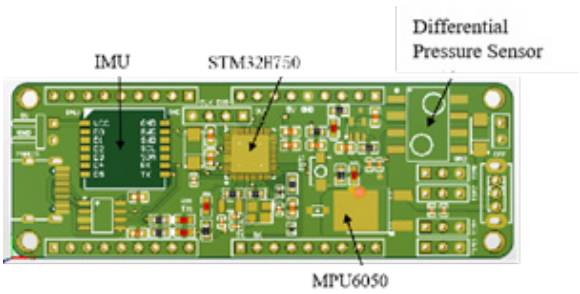

Figure 3: Small vehicle flight control board.

Flight Vehicle Simulation Analysis

As shown in Figure 4, the vehicle needs to fly over a distance of 26.45m and successfully hit a target with an effective range of only 196cm 2 after a long-distance flight. Effective hitting has high requirements on the attitude of the vehicle, which needs to have a more accurate flight trajectory and no rotating, flipping and other movements on the way. A series of finite element analyses are performed on the vehicle in order to obtain a vehicle with ideal flight attitude and sufficient strength. In order to ensure that the vehicle travels in a straight line on a preset trajectory as it is launched from the launcher and that the direction of velocity follows the trajectory without roll-axis rotation as it ejects from the launcher, it is necessary to avoid resonance of the vehicle during the ejection process. Although vibration cannot be completely eliminated, its effects can be reduced. Multiple angularly controllable rudder wings on the vehicle are used to adjust the attitude during air gliding, but there is no need to consider the rudder wing attitude in the modal analysis. Due to the complexity of delineating the mesh and applying constraints between multiple components, we simplified the adjustable rudder wing and the shell into a single unit by merging the rudder wing and the fixed wing into a single unit for analysis. As shown in Figure 5.

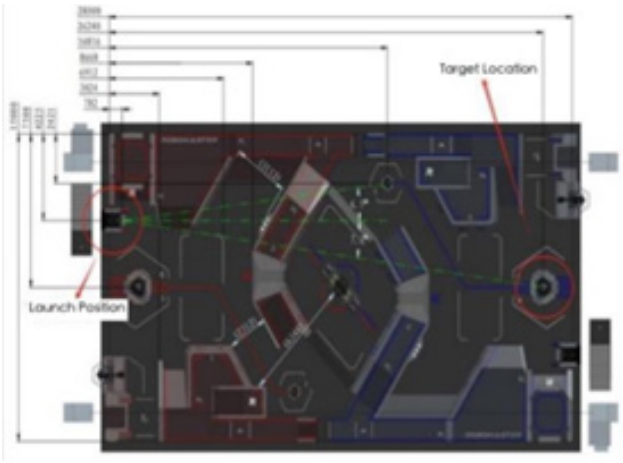

Figure 4: Schematic diagram of the working site of the flying machine.

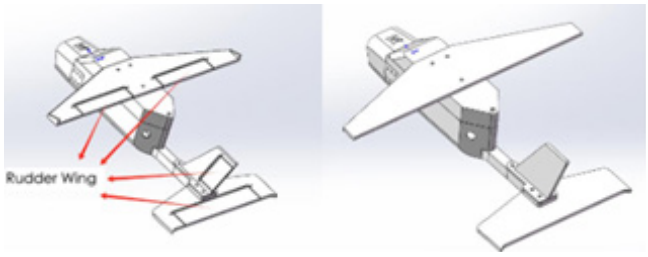

Figure 5: Comparison between before and after model simplification.

The aircraft as a whole is 3D printed, the material is PLA, the aircraft head material is TPU. Due to the performance of the PLA material is related to the production, this paper adopts the Top Bamboo PLA consumables related parameters to analyse, TPU is

the same, set the material parameters as shown in Figure 6. When meshing, the previous contact surfaces were contact matched, the mesh size was set to 1mm, the physical environment was set to mechanical, the transition was set to slow, and the span angle centre was set to fine (Figure 7). To obtain a better mesh, try using the hexahedron dominated method. However, at least one of the geometries was chosen to have a smaller volume-to-surface-area ratio, resulting in fewer proportions of hexahedra or poorly shaped cells (Figure 8). Reducing the mesh size significantly increases the analysis time and the mesh remains undivided. Therefore, instead, a tetrahedral approach is used, choosing a second-order tetrahedron and using patch fitness shapes. As shown in Figure 9, only the lower face of the vehicle is pushed out by the propulsion block on the launcher when it is on the launch track, so when setting the constraints for the modal analysis, a fixed constraint is imposed on the lower face, ignoring the effect of gravity, and the other directions are free.

Figure 6: Flight vehicle material parameters.

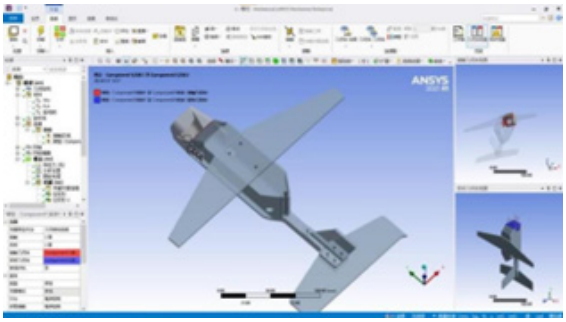

Figure 7: Contact settings.

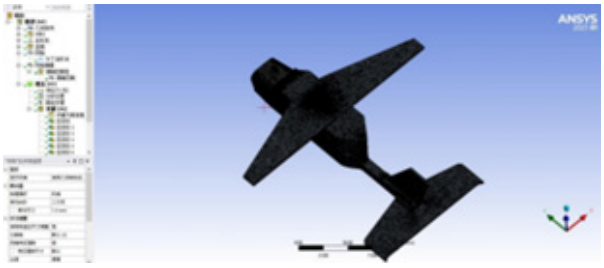

Figure 8: Grid division results.

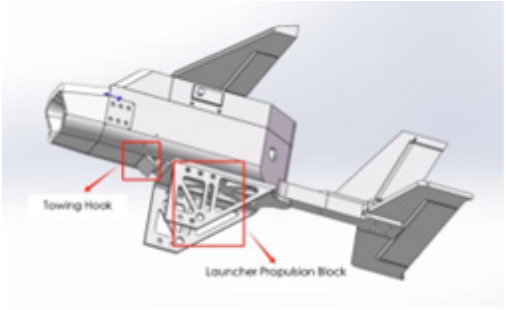

Figure 9: Schematic of vehicle propu.

Pre-launch modal analysis

Calculating the twelfth order intrinsic frequency, the results are 88.88Hz, 91.32Hz, 208.38Hz, 212.33Hz, 243.21Hz, 418.53Hz, 442.66Hz, 485.22Hz, 658.37Hz, 659.1Hz, 682.05Hz, 705.21Hz. These frequencies represent the natural frequencies of the vehicle in different modes of vibration (Figure 10). These frequencies can help determine if the vehicle resonates during ejection, which can affect its flight stability. Further tests using other settings of the CFD grid, changing the grid size and other methods, the calculated twelfth-order intrinsic frequency are not much different (Figure 11). Therefore, the experimental results of the grid are large due to the error. The cloud of vibration patterns of each order is called out, as shown in Figure 12. From the cloud of vibration patterns, it can be seen that the deformation is mainly concentrated in the two sides of the main wing and the tail wing of the vehicle. This means that at these frequencies the main and tail fins are susceptible to vibration. If vibration of a certain order of intrinsic frequency occurs during flight or in other complex environments, local reinforcement, especially in the main and tail regions, can be performed based on these results to improve the vibration resistance of the vehicle.

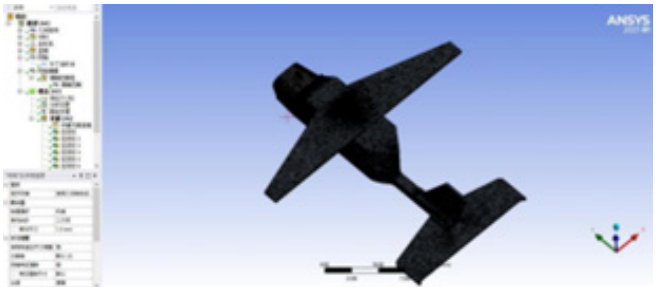

Figure 10: Grid division results.

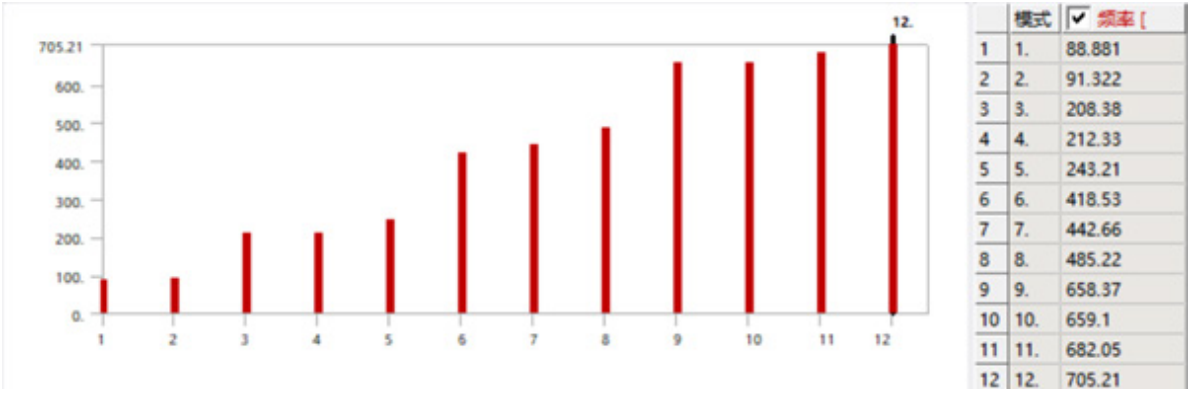

	模式	频率 [
1	1.	88.881
2	2.	91.322
3	3.	208.38
4	4.	212.33
5	5.	243.21
6	6.	418.53
7	7.	442.66
8	8.	485.22
9	9.	658.37
10	10.	659.1
11	11.	682.05
12	12.	705.21

Figure 11: Twelfth order intrinsic frequency.

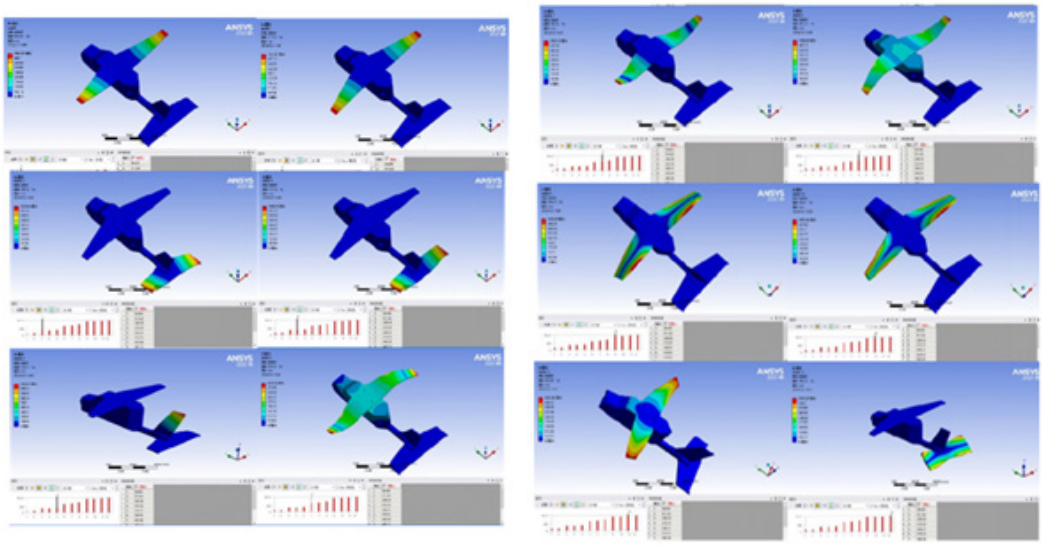

Figure 12: Schematic illustration of the vibration patterns of each order: (a) 1-6th order vibration patterns; (b) 7-12th order vibration patterns.

The vibrations transmitted during the operation of the motor are very complex and cannot be analysed directly in a modal analysis. Therefore, the vibration frequency range during motor operation needs to be measured by practical tests and analysed in comparison with the intrinsic frequency of the vehicle. If the operating speed range of the motor avoids the intrinsic frequency of the vehicle, resonance can be avoided by adjusting the time domain response of the control system. If avoidance is not possible, the position of the internal components of the vehicle needs to be adjusted to change the mass distribution and intrinsic frequency of the vehicle in order to avoid resonance.

Flow field analysis during flight

Since the success of the vehicle in hitting the target is conditional on the head hitting the top armour plate, there are certain requirements on the attitude of the vehicle in the air, which require the vehicle not to undergo a large deflection in the pitch axis direction. Therefore, there is a need to analyse the flow field of the vehicle and to investigate the forces on the vehicle while it is flying in the air.

Classification of airborne flight attitude: Figure 13 shows when the vehicle attitude is parallel to the direction of velocity (case one). Figure 14 shows the vehicle attitude at an angle of 30 degrees to the direction of velocity (later referred to as case II).

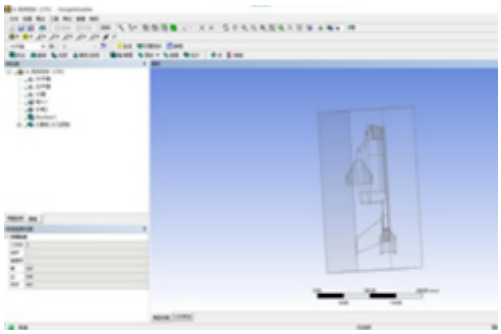

Figure 13: Vehicle attitude parallel to the direction of velocity.

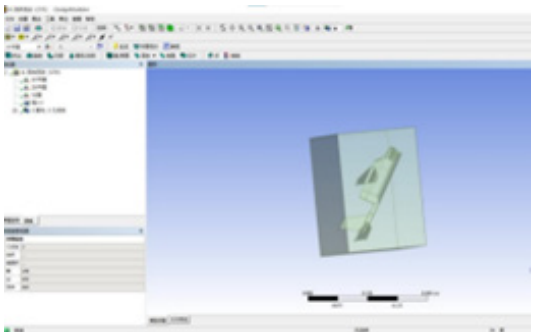

Figure 14: Vehicle attitude at an angle of 30 degrees to the direction of velocity.

Simulation analysis:

A. Vehicle attitude parallel to the direction of velocity: The delineation mesh size is 5mm, the delineation method is hexahedron dominant, and the delineated mesh is shown in Figure 15 with good mesh quality. The fluid material is set to be air at 25 °C and the solution results are shown in Table 1 & 2. The boundary flow data from CFX show the mass flow rate and momentum changes of the vehicle at each boundary condition. Default Domain. The Default boundary has no matter passing through it, but shows a certain amount of momentum in the X, Y and Z directions. The In boundary shows a positive mass flow, indicating that material enters the system and the main momentum is concentrated in the Y and Z directions. The Out boundary, on the other hand, shows a negative mass flux, indicating that the substance leaves the system with maximum momentum in the Y direction. Negative mass flow at the Wall boundary indicates a loss of material, with the main momentum concentrated in the Y direction. These data help to understand the fluid behaviour and momentum distribution of the vehicle under different boundary conditions.

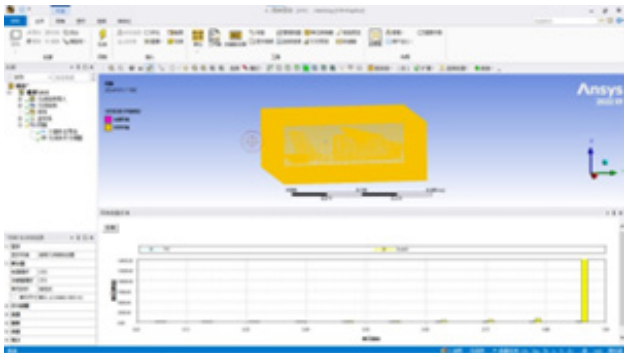

Figure 15: Grid division (case I).

Table1: Boundary flow of CFX (case I).

Location	Type	Mass Flow	Momentum		
			X	Y	Z
Default Domain Default	Boundary	0.00E+00	2.16E-04	3.00E-01	-3.67E-02
In	Boundary	6.71E-01	-7.01E-08	-1.04E+01	-1.04E+01
Out	Boundary	-6.57E-01	-3.57E-04	9.68E+00	2.67E-02
Wall	Boundary	-1.43E-02	9.61E-05	4.12E-01	9.86E-03

Table2: Force and torque of CFX (Case I).

Location	Type	X	Y	Z
Default Domain Default	Pressure Force	-1.45E-04	-2.69E-01	-3.67E-02
	Viscous Force	-7.06E-05	-3.14E-02	-1.04E+01
	Total Force	-2.16E-04	-3.00E-01	2.67E-02
	Pressure Torque	-1.21E-02	1.20E-04	-1.18E-03
	Viscous Torque	-1.81E-04	3.86E-06	9.12E-06
	Total Torque	-1.22E-02	1.24E-04	-1.17E-03

The CFX force and torque data show the forces on the vehicle under pressure and viscous action. The pressure forces are mainly concentrated in the Y-direction, while the viscous forces are greatest in the Z-direction. The distribution of the total force shows that the force in the Y direction has the greatest influence. The pressure torque and viscous torque are largest in the X-direction, which is still the main direction of influence in the total torque, albeit with smaller values. The results of the analysis can provide a reference for the structural design and optimisation of the vehicle, especially in coping with the effects of forces and torques in the Y and X directions.

From Table 1 & 2, it can be seen that the air has a moment on the vehicle in the-x direction, a moment that is exacerbated by the downward deflection of the vehicle's elevation angle. So, the moment of the vehicle subjected to the fluid in attitude parallel to the direction of velocity does not resist the unbalance moment due to its own centre-of-mass deflection, but instead exacerbates the change in attitude on pitch. Figure 16 the flow diagram shows a high-speed region above the head of the vehicle and a low-speed region below the head. The velocity field at the corner above the

head is obviously larger than the surrounding area, which indicates that the geometric design of this part of the aircraft is not reasonable and does not conform to the streamline shape, which may increase the drag force during the flight, and should be optimised in the subsequent design. From Figure 17, it can be seen that since the wing itself is not convex and concave, there is no obvious difference between the pressure fields on the upper and lower surfaces of the wing in the pressure cloud diagram, so the wing cannot provide lift. If we want the wing to provide some lift, the wing cross section should be changed to an up-convex and down-flat or up-convex and down-concave structure.

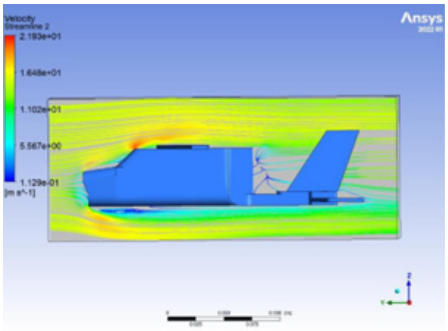

Figure 16: Flow chart.

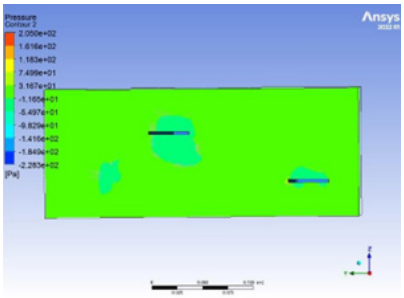

Figure 17: Pressure cloud on the wing cross-section of the aircraft.

The attitude of the aircraft is at an angle of 30 degrees to the direction of velocity.

The mesh size is 5mm and the method is hexahedron dominated. The mesh is divided as follows. The fluid material is set to be air at 25 °C and the results of the solution are as follows: Boundary flow data from CFX show the change in fluid momentum for the vehicle at an attitude angle of 30 degrees from the direction of velocity. The Default Domain Default boundary shows major momentum concentrated in the Y and Z directions with 1.2661e+1 and 6.2879e+0, respectively, suggesting a large momentum change in these directions. The In boundary shows negative mass flow and momentum mainly in the Y and Z directions and the Out boundary shows zero mass flux, but there are still momentum changes in the Y and Z directions. The Wall boundary shows a positive mass flux, with the main momentum concentrated in the Y and Z directions, suggesting that there is an accumulation of material (Table 3). CFX forces and torques (case II) for the vehicle under pressure and viscous effects. The pressure force is mainly concentrated in the Z-direction and is negative, indicating that the pressure force is greatest in that direction. The viscous force is also largest in the Z direction, but the value is much smaller than the pressure force. The distribution of the total force shows that the total force is largest in the Z direction and the pressure torque is also larger in the X direction, indicating that the vehicle needs to pay special attention to the force in the Z direction and the torque in the X direction in this attitude. The total torque is mainly concentrated in the X-direction and the pressure torque has a significant effect in the X-direction, although the viscous torque is small. As can be seen from Table 3 & 4, compared to when the velocity direction is parallel to the attitude, the fluid moment at this point in time is hindering the vehicle attitude deflection, indicating that the vehicle configuration has a self-correcting function when a certain amount of vehicle attitude deflection occurs.

Table3: Boundary flow for CFX (Case II).

Location	Type	Mass Flow	Momentum		
			X	Y	Z
Default Domain Default	Boundary	-9.82E-01	1.95E-02	1.27E+01	6.29E+00
In	Boundary	-2.27E-01	-2.05E-02	3.44E+00	1.94E+00
Out	Boundary	0.00E+00	2.62E-03	2.85E-01	1.23E+00
Wall	Boundary	1.21E+00	-3.62E-09	-1.64E+01	-9.46E+00

Table 4: Force and torque for CFX (case II).

Location	Type	X	Y	Z
Default Domain Default	Pressure Force	-2.53E-03	-2.70E-01	-1.23E+00
	Viscous Force	-9.48E-05	-1.46E-02	-1.97E-03
	Total Force	-2.62E-03	-2.85E-01	-1.23E+00
	Pressure Torque	6.27E-02	-1.69E-03	6.27E-05

	Viscous Torque	7.83E-06	1.94E-06	-4.60E-06
	Total Torque	6.28E-02	-1.69E-03	5.81E-05

Landed collision analysis

Due to the large flight speed of the vehicle, the landing speed is about 15m/s, the landing process will encounter a large impact (Figure 18). In order to reduce the impact of the stress generated by the damage to the vehicle, we will simulate the stress distribution of the vehicle in different attitudes after the landing to find the maximum material extrusion, shear stress of the region, by changing the landing position, the mechanical structure of the vehicle or the material to avoid damage during the landing process of the vehicle. Damage during landing by changing the landing position, the mechanical structure of the vehicle or the material. In Workbench, using the LS-DYNA analysis system, set the required material properties in the engineering data as shown in Table 5. Import the model from Solid works into 'Geometry' and add the material properties to the corresponding structure. The front part of the vehicle is made of flexible TPU, so that it can better mitigate the huge impact when landing on the front part; the fuselage of the vehicle is made of PLA, which is made by 3D printing process; and the ground is paved with 5mm thick rubber, as shown in Figure 19. Set the friction in the geometry interaction.

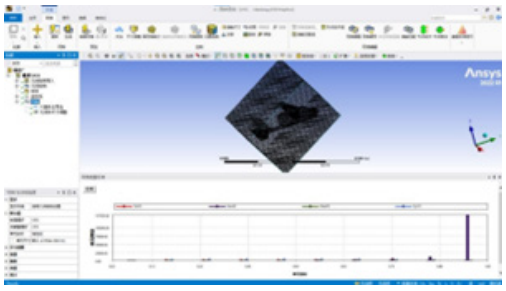

Figure 18: Grid division (case II).

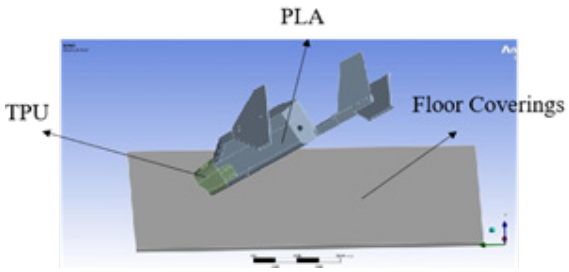

Figure 19: Material distribution.

Table 5: Material properties.

Material	Density(g/cm^3)	Young's Modulus (MPa)	Poisson's Ratio
PLA	1.25	2750	0.35
TPU	1.2	1000	0.48
Floor Coverings	1.2	500	0.45

The friction coefficient is 0.75 and the power coefficient is 0.70. Insert geometry size adjustment, select the geometry and set the cell size to 5.0mm, as shown in Figure 20. Set the landing speed before and after as shown in Table 6. Set the standard earth gravity, select the floor bottom for fixed support with the analysis time of 0.08. Simulation of vehicle equivalent force distribution. The following Figure 21 shows the front landing equivalent force analysis profile (Figure 22). As can be seen in Figure 23, the head and front fuselage portion of the vehicle has the highest stresses when landing at the front, especially in the area in contact with the ground, showing higher stress values that gradually increase from green to red. Figure 1 shows a concentration of stress in the bottom regions of the head and forward fuselage of the vehicle, with a colour close to red, indicating that these regions have higher stress values and bear the main impact forces. The range of stress values can be seen in the legend, with the stress values for the head and forward fuselage sections being at the high end of the legend, close to the red region and the other sections being relatively less stressed, with the colours gradually transitioning to blue, suggesting that less stress was applied to these areas.

Table 6: Velocity.

Statuses	X component (m/s^2)	Y component (m/s^2)	Z component (m/s2)
Front Landing	0	8.66	-5
Tail Landing	0	4.33	-2.5

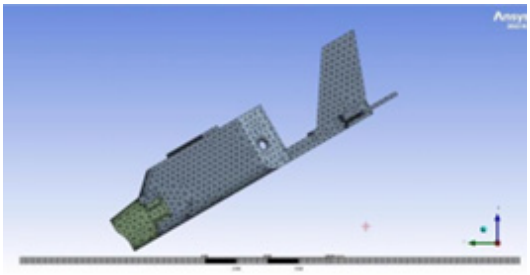

Figure 20: Grid division.

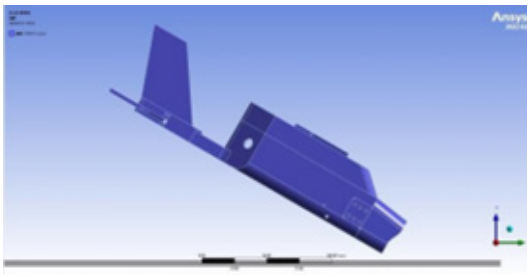

Figure 21: Head landing condition.

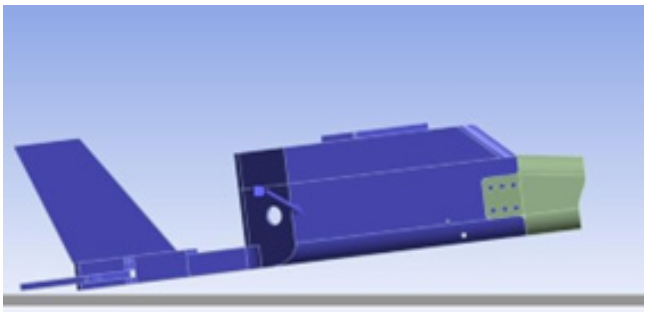

Figure 22: Tail landing condition.

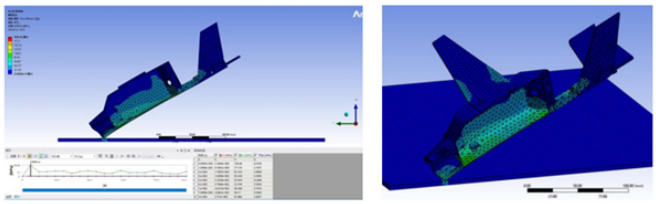

Figure 23: Front landing stress diagram.

The stress gradient gradually decreases from the front to the rear of the vehicle, with the stress values gradually transitioning from red to green and blue, indicating that the front portion of the vehicle is subjected to a larger impact, while the rear portion of the vehicle is subjected to less stress. Figure 2 further demonstrates the stress distribution of the vehicle during a forward landing, showing finer mesh delineation, especially in the areas of stress concentration, where the mesh fineness is higher to capture the stress distribution more accurately. The finer mesh delineation results in clearer areas of stress concentration, with well-defined areas of stress concentration in the head and forward fuselage showing red areas, indicating that the stresses are highest in these areas. The specific stress values can be seen from the scale in the figure and this information enables a more accurate understanding of the stresses in different areas, assessment of the stresses on the vehicle during landing, and identification of structural areas that need to be strengthened. In summary, the concentration of stresses in the head and forward fuselage of the vehicle during forward landing requires structural reinforcement and material optimisation of these areas to ensure the reliability and durability of the vehicle in practical use.

From Figure 24, it can be seen that when the vehicle lands on its tail, the stresses in the tail and tail section are the highest, especially in the region of contact with the ground. The stress values gradually increase from green to yellow, showing higher stress concentration areas. The mesh is finely delineated, especially in the areas of stress concentration and the higher mesh fineness helps to capture the stress distribution more accurately. The specific stress values show that the maximum stress value in the tail reaches 1.0724e+06 Pa, the medium stress value in the green area ranges from 5.3188e+05 Pa to 7.9186e+05 Pa, and the stress value in the blue area is smaller and lower than 5.3188e+05 Pa. The collision simulation results of this small craft in two landing attitudes are analysed. The maximum stress in the front landing is 199.46 MPa, and the maximum stress in the tail landing is 19.287 MPa. From the distribution of the stresses, it can be found that there is a concentration of stress in the part connecting the fuselage and the tail wing of the craft. The stresses at the bottom of the fuselage body during the forward landing are also large, at 88.65 MPa, and it is considered to modify the mechanical structure or material of these parts to avoid damage during the landing of the vehicle.

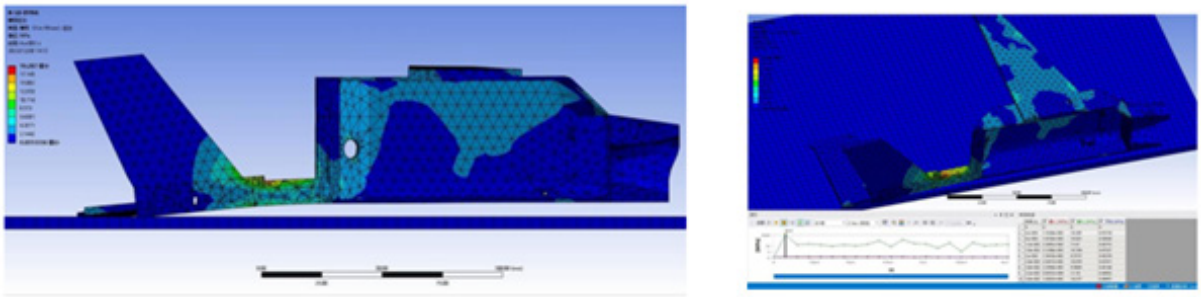

Figure 24: Tail landing stress diagram.

Ground state subjected to static analysis

Due to the complexity of the site environment, when the vehicle completes the flight process and is in the ground state, it is prone to being pushed, crushed and extruded by other robots. In order to reduce the damage caused by these external forces on the vehicle, we will simulate the force on the vehicle after it has landed, and analyse the stress and deformation of the various parts, search for the location of the weak strength, and make target reinforcement by means of altering the geometrical structure or the material.

Modelling: Considering that the fundamental purpose of the ground stress analysis is to verify the structural strength and after preliminary analysis, we believe that the most likely to be damaged when the vehicle is subjected to pressure are the wing and tail sections, we simulated the two most likely to be damaged typical cases. As shown in Figure 25. In one case, the vehicle tipped over and the wheels crushed the wing, as shown in Figure 25(a). We will analyse the strength of the wing and tail in this case. Secondly, the wheels push the vehicle against the wall and squeeze the wing

together with the wall, as shown in Figure 25(b). It should be noted that this situation seems to be more extreme and has less probability of occurring in reality, but after a simple force analysis we conclude that the wing has the maximum force in this state (Figure 26). The model in this state is chosen for the purpose of calibrating the strength of the wing.

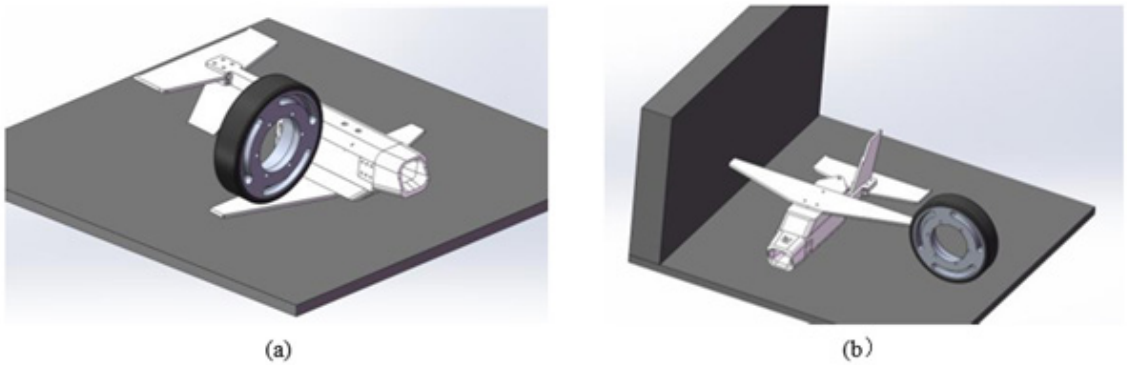

Figure 25: Force assumptions.

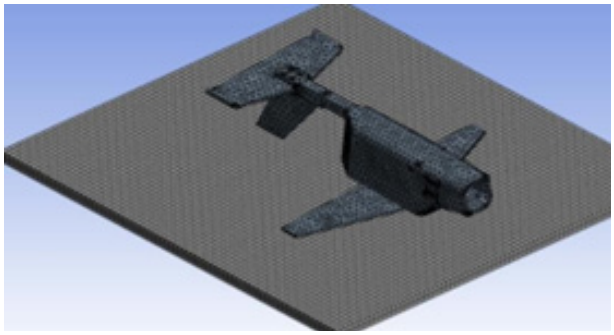

Figure 26: Scene 1 meshing.

Simulation Analysis of Scene 1: Plot grid size 5mm. standard earth gravity, ground displacement constraints. Loads: X=50N, Y=10N, Z=10N.

A. Stress analysis: The maximum stress on the wing at this point is about 2.7MPa, while the stress on the tail is smaller and since there is a small space below the wing from the ground, it is necessary to analyse whether the strength of the wing is sufficient. At the same time, the fuselage is also subjected to a small amount of stress, but it will not affect its internal structure and important components (Figure 27).

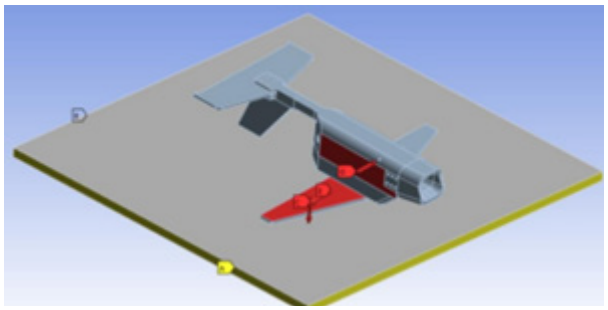

Figure 27: Scene 1 applying constraints.

B. Deformation analysis: The maximum deformation at this point is about 0.5mm, which occurs near the contact point between the wing and the crushed area, and the deformation is within the elastic deformation range of the material (Figure 28).

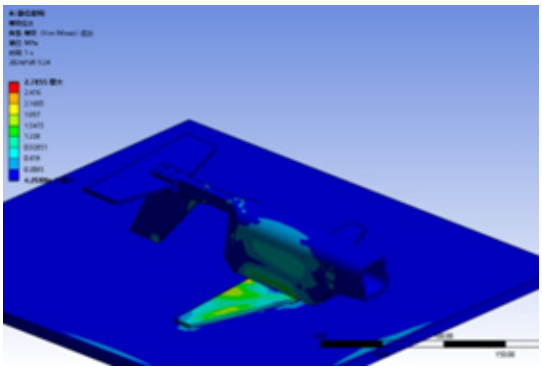

Figure 28: Scene 1 stress analysis results.

Scene 2 simulation analysis: Same as Scenario I. Standard earth gravity, wall fixed support. Load: Z= 20N.

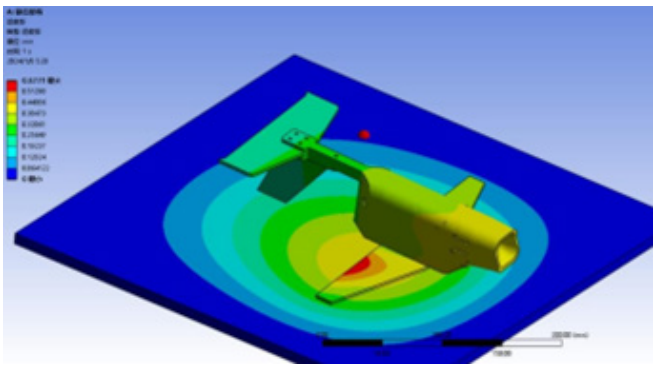

Figure 29: Deformation analysis result of scene 1.

A. Stress analysis: The maximum stress on the wing at this time is about 1.01MPa, which is smaller than the previous state, and the stress on the wing surface is more symmetrical, and it can be seen that the tip of the wing against the wall has the highest stress (Figure 29&30).

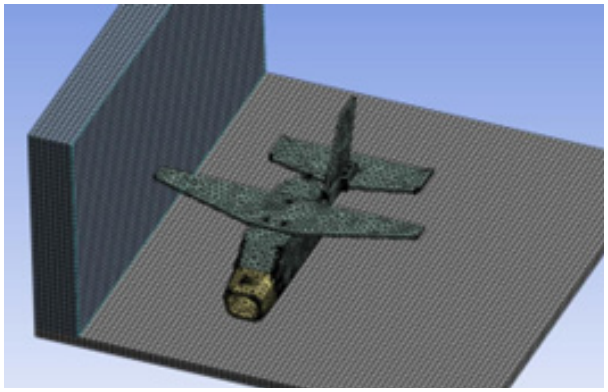

Figure 30: Scene 2 Grid division.

B. Deformation analysis: The maximum deformation is about 0.004mm, which is very small. The deformation of the wing extruded by the wheels is relatively large, because part of the deformation is generated by the self-weight, but it is not obvious on the wall side because it is in contact with the wall (Figure 31).

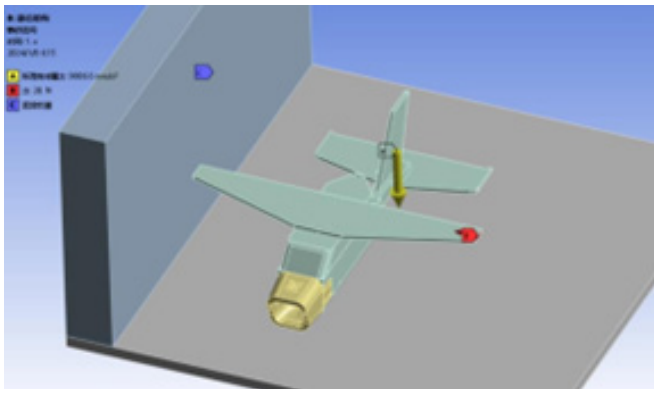

Figure 31: Imposing constraints in scene 2.

In Scene 2, the stresses and deformations of the vehicle are mainly concentrated in the part of the wing in contact with the wall. The stress value reaches a maximum of 1.0831e+07Pa, while the maximum deformation is 8.2462e-3m. The gradual decrease of stress and deformation from the contact area to the centre of the fuselage indicates that the contact area of the wing with the wall surface is subjected to the main stress and deformation (Figure 32 & 33). In order to ensure the reliability and durability of the vehicle under such conditions, structural reinforcement and material optimization of the wing-wall contact part are required to reduce the effects of stresses and deformations on the overall performance of the vehicle.

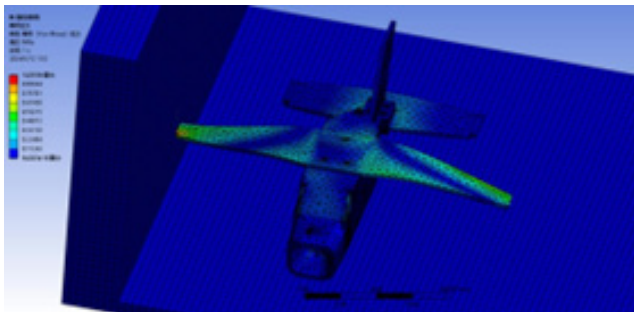

Figure 32: Scene 2 Stress analysis results.

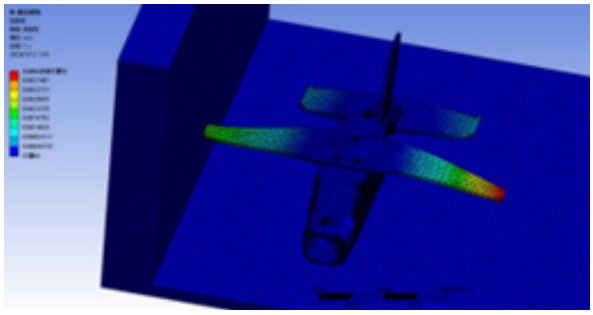

Figure 33: Deformation analysis result of scene 2.

Conclusion

In this paper, the dynamics and aerodynamic characteristics of a small guided vehicle during ejection are analysed in detail by finite element method. The study uses ANSYS software to simulate and analyse the modal state of the vehicle before launch, the flow field during flight and the landing collision scenarios. The results show that the intrinsic frequencies of the vehicle in different states are 88.88Hz, 91.32Hz, 208.38Hz, etc., And the main stresses are concentrated in the head, wing and tail regions of the vehicle. In the flight attitude analysis, it is found that the vehicle has a self-correction function when it makes an angle of 30 degrees with the direction of velocity, which indicates that the vehicle structure can adjust itself at a certain attitude deflection. In addition, in the landing collision analysis, the maximum stress of the front landing is 199.46MPa and the maximum stress of the tail landing is 19.287MPa and the main stresses are concentrated in the fuselage and the tail connection part. Finally, the static stresses of the vehicle in the ground state were analysed, and targeted structural strengthening suggestions were made to improve the reliability and durability of the vehicle.

References

1. Yiran S, Yingshuo C, Qi J, Yilin W (2013) Analysis of the development and performance of typical foreign cruise missiles. Scuderia Missile 2: 37-40.
2. Sutthison D, Wongkamchang P, Sukuprakarn N (2022) Aerodynamic studies of small box-wing unmanned aerial vehicle using CFD. Journal of Physics: Conference Series 2235(1): 012070.
3. Aditya A, Srinivas G (2019) Recent evolution of low Reynolds number flyers: Paving way for Micro Air Vehicles (MAV). Journal of Physics: Conference Series 1172(1): 012034.

4. Serré R, Gourdain N, Jardin T, Jacob MC, Moschetta JM, et al. (2019) Towards silent micro-air vehicles: Optimization of a low Reynolds number rotor in hover. International Journal of Aeroacoustics 18(8): 690-710.
5. Ang Hai-Song, Xiao Tian-Hang, Zheng Xiang-Ming (2018) Low Reynolds number, non-constant aerodynamic design and analysis of micro air vehicle. Unmanned Systems Technology 1(04): 17-32.
6. Zhang Fuxing, Zhu Rong, Zhou Zhaoying (2008) Experimental study on aerodynamic characteristics of flexible wing micro air vehicle. Journal of Aeronautics 6: 1440-1446.
7. Yang Wenqing, Song Penfeng, Song Wenping, Chen Lili (2015) Research progress and challenges of aerodynamic problems in bionic micro flapping wing vehicle. Experimental Fluid Mechanics 29(3): 1-10.
8. Yang Shuli, Song Wenping, Song Penfeng, Shao Limin (2006) Aerodynamic characteristics of the wing of a miniature flapping wing vehicle. Journal of Northwestern Polytechnical University 24(6): 768-773.
9. Lu Ping (1996) Nonlinear trajectory tracking guidance with application to a launch vehicle. Journal of Guidance, Control and Dynamics 19(1): 99-106.
10. Seywald Hans (1994) Neighbouring optimal control-based feedback law for the advanced launch system. Journal of Guidance, Control and Dynamics 17(6): 1154-1162.
11. Lu Ping (2007) Rapid optimal multi-burn ascent planning and guidance. AIAA guidance, Navigation and Control Conference and Exhibit, Hilton Head, South Carolina, USA.
12. Brown KR, Harrold EF, Johnhson GW (1970) Some new results on space shuttle atmospheric ascent optimization. AIAA Paper, pp. 70-978.
13. Ingram HL (1972) Closed-form solutions for atmospheric flight with applications to shuttle guidance. NASA TM, USA.
14. Kelly WD (1992) Formulation of aerodynamic quantities for minimum hamiltonian guidance. AIAA Paper, pp. 92-4380.
15. Dickey LR (1964) Guidance applications of linear analysis. Marshall Space Flight Centre, Alabama, USA.
16. Bradt JE, Jessich MV, Hardtla JW (1987) Optimal guidance for future space applications. AIAA Paper, Monterey, California, pp. 87-2401.
17. Cramer EJ, Bradt JE, Hardtla JW (1990) Launch flexibility using NLP guidance and remorte wind sensing. AIAA Paper, USA, pp. 90-3330.
18. Hanson J, Shrader M, Cruzen C (1995) Ascent guidance options. The Journal of the Astronautical Sciences 43(3): 307-326.
19. Leung MSK, Calise AJA (1992) Hybrid approach to near-optimal launch vehicle guidance, AIAA Paper, pp. 92-4304.
20. Calise AJ, Melamed N, Lee Seungjae (1998) Design and evaluation of a three-dimensional optimal ascent guidance algorithm. Journal of Guidance, Control and Dynamics 21(6): 867-875.
21. Gath P, Calise A (1999) Optimization of launch vehicle ascent trajectories with path constraints and coast arcs. AIAA Paper, pp. 99-4308.
22. Jezewski DJ (1972) Optimal analytic multiturn trajectories. AIAA Journal 10(5): 680-685.
23. Bown RL (1975) Return-to-launch-site trajectory shaping. NASA-CR, USA.
24. Carter JF, Bown RL (1975) Space shuttle three main engine return to launch site abort. NASA-CR-150968, USA.
25. Sponagle Steven, J Fernandes, Stanley T (1989) Space shuttle guidance for multiple main engine failures during first stage. Journal of Guidance, Control and Dynamics 12(6): 880-885.
26. Kishi MW, Gavert DE, Dee YT (1980) Development and performance evaluation of the space shuttle vehicle guidance and control for return to launch site aborts. AIAA Paper 1980-907, Proceedings of the American Institute of Aeronautics and Astronautics, International Meeting and Technical Display on Global Technology 2000, Baltimore, USA.
27. Dutton Kevin E (1994) Optimal control theory determination of feasible return-to-launch-site aborts for the HL-20 personnel launch system vehicle. NASA Langley Research Centre NASA TP-3449, USA.
28. Stanley DO, Powell RW (1991) Abort capabilities of rocket-powered single-stage launch vehicles. Journal of Spacecraft and Rockets 28(2): 184-191.
29. Chuang CH, Ledsinger Laura A (1996) First and second variation analysis for return to launch site guidance. AIAA Paper 1996-3426, Proceedings of the AIAA Atmospheric Flight Mechanics Conference, San Diego, California, USA, pp. 534-542.
30. Dukeman Greg A (2002) Profile-following entry guidance using linear quadratic regulator theory. AIAA Guidance, Navigation and Control Conference and Exhibit, AIAA-2002-4457, USA.